Spectroscopic thermo-elastic optical coherence tomography for tissue characterization

Deen, Aaron Doug; van Beusekom, Heleen M.M.; Pfeiffer, Tom; Stam, Mathijs; Kleijn, Dominique D.E.; Wentzel, Jolanda; Huber, Robert; van der Steen, Antonius F.W.; Van Soest, Gijs; Wang, Tianshi

Important note
To cite this publication, please use the final published version (if applicable).
Please check the document version above.

Spectroscopic thermo-elastic optical coherence tomography for tissue characterization

AARON DOUG DEEN,[1] (iD) HELEEN M. M. VAN BEUSEKOM,[1] TOM PFEIFFER,[2] MATHIJS STAM,[1] DOMINIQUE DE KLEIJN,[3] JOLANDA WENTZEL,[1] ROBERT HUBER,[2] (iD) ANTONIUS F. W. VAN DER STEEN,[1,4,5] GIJS VAN SOEST,[1] AND TIANSHI WANG[1,*]

[1]*Department of Cardiology, Erasmus University Medical Center, P.O. Box 2040, Rotterdam 3000 CA, The Netherlands*
[2]*Institut für Biomedizinische Optik, Universität zu Lübeck, Peter-Monnik-Weg 4, 23562 Lübeck, Germany*
[3]*University Medical Center Utrecht, Heidelberglaan 100, 3584 CX Utrecht, The Netherlands*
[4]*Shenzhen Institutes of Advanced Technology, Chinese Academy of Sciences, 518055 Shenzhen, China*
[5]*Department Imaging Science and Technology, Delft University of Technology, Delft 2600 AA, The Netherlands*
[*]*t.wang.1@erasmusmc.nl*

Abstract: Optical imaging techniques that provide free space, label free imaging are powerful tools in obtaining structural and biochemical information in biological samples. To date, most of the optical imaging technologies create images with a specific contrast and require multimodality integration to add additional contrast. In this study, we demonstrate spectroscopic Thermo-elastic Optical Coherence Tomography (TE-OCT) as a potential tool in tissue identification. TE-OCT creates images based on two different forms of contrast: optical reflectance and thermo-elastic deformation. TE-OCT uses short laser pulses to induce thermo-elastic tissue deformation and measures the resulting surface displacement using phase-sensitive OCT. In this work we characterized the relation between thermo-elastic displacement and optical absorption, excitation, fluence and illumination area. The experimental results were validated with a 2-dimensional analytical model. Using spectroscopic TE-OCT, the thermo-elastic spectra of elastic phantoms and tissue components in coronary arteries were extracted. Specific tissue components, particularly lipid, an important biomarker for identifying atherosclerotic lesions, can be identified in the TE-OCT spectral response. As a label-free, free-space, dual-contrast, all-optical imaging technique, spectroscopic TE-OCT holds promise for biomedical research and clinical pathology diagnosis.

1. Introduction

Optical imaging techniques have proven to be powerful tools in providing information on tissue structure and molecular composition with high spatial and temporal resolutions. Typically, optical imaging technologies rely upon a single form of imaging contrast and offer a single, specific type of information on the tissue sample. Microscopy implementations include the chemical information offered by fluorescence, Raman and multiphoton microscopy, optical reflectance visualized by confocal microscopy and tissue elasticity shown by Brillouin microscopy [1–4]. To further expand imaging capabilities, systems consisting of multiple modalities have been demonstrated which create images containing multiple imaging contrasts simultaneously. However, this normally requires the integration of various imaging modalities [5,6]. Another key technical concern of note involves the use of contrast agents in imaging modalities where signal detection is limited. Due to the general toxicity of common contrast agents, further investigation is required into their safety and adverse effects [7–10]. As a result of these factors, development of new label-free and free-space hybrid imaging modalities has been desirable in the field of optical imaging.

In the last decade, photoacoustic imaging (PAI) has emerged as a hybrid imaging technique, bearing potential for research and clinical diagnostic applications [11,12]. PAI employs pulsed laser to induce thermoelastic deformation in tissue. Following the absorption of the laser pulse, the tissue undergoes rapid thermal expansion which generates internal thermoelastic stresses and acoustic waves, then slowly relaxes over tens of microseconds during a period referred to as, 'quasi-steady-state equilibrium' [13]. PAI uses ultrasound transducers to detect the consequent acoustic wave to achieve tissue specific imaging contrast. This allows for simultaneous visualization of tissue components depending on optical absorption, and tissue structure depending on the acoustic properties of the tissue [14,15]. The optical contrast imaging offered by PAI, has thus been applied in a number of research areas from changes in vasculature to lipid identification [16–20]. However, conventional PAI typically requires a contact medium between the transducer and sample to ensure propagation of the acoustic wave. To achieve non-contact imaging, photoacoustic remote sensing (PARS) has been proposed [21], in which the ultrasound detection is replaced by optical sensing. However, this tradeoff for all-optical detection results in the loss of depth information and the ultrasound imaging contrast.

Optical coherence tomography (OCT) is an all-optical imaging technique which uses low-coherence interferometry to provide volumetric imaging of tissue microstructure, having widespread applications, most notably in ophthalmology, cardiology, and oncology [22–25]. The imaging contrast of OCT depends on the optical scattering and reflection of the sample. Though OCT offers non-contact, high-resolution imaging, it conventionally shows only the tissue structure and surface optical reflectance in its microscopy format [26,27]. Functional extensions of OCT have been proposed to offer additional tissue-specific contrast. For instance, polarization OCT (PS-OCT) measures changes in the polarization state of the detected light to identify tissue type such as collagen and muscle [28]. Spectroscopic OCT (SOCT) can extract the spectroscopic features of the tissue within the wavelength range of the OCT laser source [29]. Phase-sensitive OCT (PhS-OCT) can detect the minute tissue displacements on a nanometer to sub-micrometer scale [30,31]. One of the major implementations of PhS-OCT has been in photothermal (PT-OCT) [32]. Traditional PT-OCT uses continuous wave (CW) laser to progressively induce temperature rise in tissue. The temperature rise further generates a photothermal signal that can be detected by PhS-OCT, thus creating additional imaging contrast that is dominated by the optical absorption.

Previously, we demonstrated the concept of thermo-elastic (TE-OCT), a hybrid imaging technique between PAI and PhS-OCT [33]. When tissue absorbs a laser pulse with a duration that is shorter than the thermal relaxation time of the tissue, thermal confinement is achieved. TE-OCT exploits this effect by combining a nanosecond pulse laser, which is used to induce TE displacement, with a megahertz phase-sensitive OCT system for detection. Like PAI, the TE-OCT signal is proportional to the locally deposited heat, and thus to the local fluence and absorption coefficient. Relying upon the laser induced, thermo-elastic expansion and making use of the technical advantages of PhS-OCT, TE-OCT offers structural OCT images and tissue type imaging simultaneously. In our previous study, we demonstrated single or dual wavelength characterization of tissue samples. In this study we advance the concept of TE-OCT towards a spectroscopic imaging setup for tissue identification. Employing a two-dimensional (2D) model and a pulse laser with a large wavelength tunable range, we extracted TE displacement spectra of phantoms and biological tissue, which can be used as a new contrast for tissue characterization. Furthermore, we acquired high-speed TE-OCT images of atherosclerotic plaque, in which the lipid, collagen and elastin tissue components can be identified by imaging at selected salient wavelengths.

2. Materials and methods

2.1. 2D model of thermo-elastic surface displacement at steady state

The absorption of laser energy by a material produces molecular vibrations and a non-uniform temperature distribution resulting in thermoelastic deformation. For the case of nanosecond laser pulses, the temperature distribution $T(r,z)$, can be approximated by an axial symmetric function, a Gaussian radial profile and an exponentially decaying axial profile called the optical attenuation depth, D [34]:

$$T(r, z) = T_0 \, \exp\left\{-\frac{r^2}{w^2}\right\} \exp\left\{-\frac{z}{D}\right\} \tag{1}$$

$$T_0 = \frac{\Phi \mu_a}{\rho C_v} \tag{2}$$

$$D = \sqrt{3\mu_a(\mu_a + \mu_s')} \tag{3}$$

where r is the radial coordinate, z is the axial coordinate, w is the radius of the laser beam, Φ is the laser fluence, C_v is the heat capacity at constant volume, μ_a is the optical absorption coefficient, μ_s' is the reduced scattering coefficient, T_0 is the initial temperature distribution and D is the optical attenuation depth, given as the distance along the axial coordinate (z), in which the laser beam is reduced to 1/e of its initial surface intensity. It should be noted that in the case of the gel wax phantoms used in the characterization of the system, scattering is assumed negligible due to the transparency of the phantoms. In this case, the optical attenuation depth, D, is simply proportional to the absorption coefficient of the material:

$$D_{trans} = \mu_a \tag{4}$$

where D_{trans} is the optical attenuation depth for a transparent material.

The deformation in a solid body as a function of time, can be determined based on the theory of elasticity using the thermoelastic wave equation, which is detailed by Landau et al. [35]:

$$\rho \frac{\partial^2 \mathbf{u}}{\partial t^2} - \frac{E}{2(1 + \sigma)} \nabla^2 \mathbf{u} - \frac{E}{2(1 + \sigma)(1 - 2\sigma)} \nabla(\nabla \cdot \mathbf{u}) = \frac{-E\beta}{3(1 - 2\sigma)} \nabla T(r, z) \tag{5}$$

where $\mathbf{u}$ is the displacement vector, ρ is density, E is Young's modulus, σ is Poisson's ratio, and β is the thermal expansion coefficient. From Eq. (5) a complete solution for the displacements and stresses can then be derived with appropriate boundary and initial conditions following the work by Albagli et al. [36]. The initial condition assumes that the displacement, $\mathbf{u}$, equals to zero at time equal to zero. The boundary conditions then assumes that the surface of the sample is free, with the stress at the surface equal to zero. In addition, the bottom of the sample is assumed fixed. Under these initial and boundary conditions, the axial, u_z and radial, u_r displacement components under steady state can be found by:

$$u_z = -\frac{1 + \sigma}{3(1 - \sigma)} D\beta T_0 \cdot$$
$$\int_0^\infty \left[\frac{(1 - 2\sigma + yz')}{(y + 1)} \exp(-yz') - \frac{(y \exp(-yz') - \exp(-z'))}{(y^2 - 1)} \right] R J_1(Ry) J_0(yr') dy \tag{6}$$

$$u_r = \frac{1 + \sigma}{3(1 - \sigma)} D\beta T_0 \cdot$$
$$\int_0^\infty \left[\frac{(2 - 2\sigma - yz')}{(y + 1)} \exp(yz') - \frac{(y \exp(-yz') - y \exp(-z'))}{(y^2 - 1)} \right] R J_1(Ry) J_1(yr') dy \tag{7}$$

where $r' = r/D$ and $z' = z/D$ are dimensionless variables, y is a symbolic variable, $R = w/D$ is an aspect ratio relating beam width, w, to effective optical attenuation depth and J_1 and J_0 are first and zero order Bessel functions.

The axial surface displacement for a Gaussian temperature distribution can then be determined by setting $z = 0$:

$$u_z = -Sg_0(R, r') \tag{8}$$

where the negative sign indicates motion towards the incoming light and

$$S = \frac{2(1 + \sigma)}{3} D\beta T_0 \tag{9}$$

$$g_0(R, r') = \int_0^\infty \frac{R^2 y}{2(y + 1)} \exp\left\{-\frac{R^2 y^2}{4}\right\} J_0(yr')dy \tag{10}$$

By combing equations (2), (3) or (4), (9) and (10) and substituting them in Eq. (8), an expression for determining the axial surface displacement resulting from an incident light pulse of Gaussian distribution while accounting for the mechanical, thermal and optical properties of the tissue, can be found:

$$u_{z=0,r'=0} = -\frac{2(1 + \sigma)}{3} \frac{1}{\sqrt{3\mu_a(\mu_a + \mu_s')}} \frac{\beta \Phi \mu_a}{\rho C_v} \int_0^\infty \frac{R^2 y}{2(y + 1)} \exp\left\{-\frac{R^2 y}{4}\right\} J_0(yr')dy \tag{11}$$

The displacement can be written as a product $A \cdot B$, where A describes the mechanical and thermal properties, while the optical properties of the tissue can be written in terms of B, including the optical attenuation depth, D, which can be simplified to D_{trans} depending on the medium turbidity:

$$A = \frac{2(1 + \sigma)}{3} \cdot \frac{\beta \Phi}{\rho C_v} \tag{12}$$

$$B = \mu_a \cdot D_{eff} \int_0^\infty \frac{R^2 y}{2(y + 1)} \exp\left\{-\frac{R^2 y^2}{4}\right\} J_0(yr')dy \tag{13}$$

It can be appreciated that the components of B, are governed by optical absorption and related to the wavelength of excitation, while the mechanical and thermal properties in A, are inherently determined by the tissue type. Thus, by selecting an appropriate wavelength, the intrinsic optical absorption of the tissue can be exploited. This offers imaging where the optical absorption at a given wavelength is then the contrast mechanism of the imaging system.

2.2. Phase-sensitive OCT system

For interrogation, a phase-sensitive OCT system based on a 1.6 MHz Fourier-domain mode locked laser (FDML) is employed. The laser has a central wavelength of 1316 nm and a wavelength sweeping range of 108 nm. The laser achieves an output power of 20 mW with a sensitivity of 102 dB and a phase stability of 0.5 nm in air. The output from the FDML laser was split in a 9:1 ratio, with 90% of the output power being sent to the sample arm, while the remaining 10% was sent to the reference arm. The reflected light from the sample arm was recombined with the light from the reference arm in a 50/50 coupler. The coherence fringes were detected by a 1.6 GHz, InGaAs balanced photodetector (Thorlabs, PDB480C-AC, U.S.) and then converted to an analogue signal with a 4 GS/s, 8-bit data acquisition (Gage, CobraMax, U.S.). The PhS-OCT system finally achieves an axial resolution of 11.9 μm and a lateral resolution of 27.0 μm. A detailed characterization of the system can be found in previous work by Wang et al. [37].

2.3. Spectroscopic TE-OCT imaging system

To induce thermo-elastic deformation, we integrated a wavelength tunable pulsed optical parametric oscillator (OPO) laser (SpitLight EVO-OPO, Innolas, Germany), into the PhS-OCT system as shown in Fig. 1(a). The pulsed laser has a wavelength tuning range of 660 - 2400

nm with pulse durations of 4 - 7 ns and repetition rates of 10 - 200 Hz. Output light from the tunable pulsed laser was attenuated to desired levels using absorptive neutral density filters then collimated with a best form lens (LBF254-100, Thorlabs, U.S.). The collimated beam was then reflected by two protected silver mirrors (PF10-03-P01, Thorlabs, U.S.) onto a second, best form lens (LBF254-040, Thorlabs, U.S.) which focuses the light through a 500 µm copper aperture (#39-895, Edmund Optics, U.S.). The light exiting the aperture was collimated with a third best form lens (LBF254-040, Thorlabs, U.S.), reflected off a 50:50 UVFS beamsplitter (BSW30, Thorlabs, U.S.) and focused on the sample through an achromatic doublet lens (AC254-030, Thorlabs, U.S.). Additionally, 1% of the light transmitted through the beamsplitter was sent to a 10 GHz, extended InGaAs photodetector (818-BB-51, Newport, U.S.) to monitor pulse-to-pulse variations in pulse energy. The interrogation OCT beam was collimated with a 1310 nm air-spaced doublet (F810APC-1310, Thorlabs, U.S.), co-aligned with the pulsed laser beam through the achromatic doublet lens and focused upon the same location on the sample.
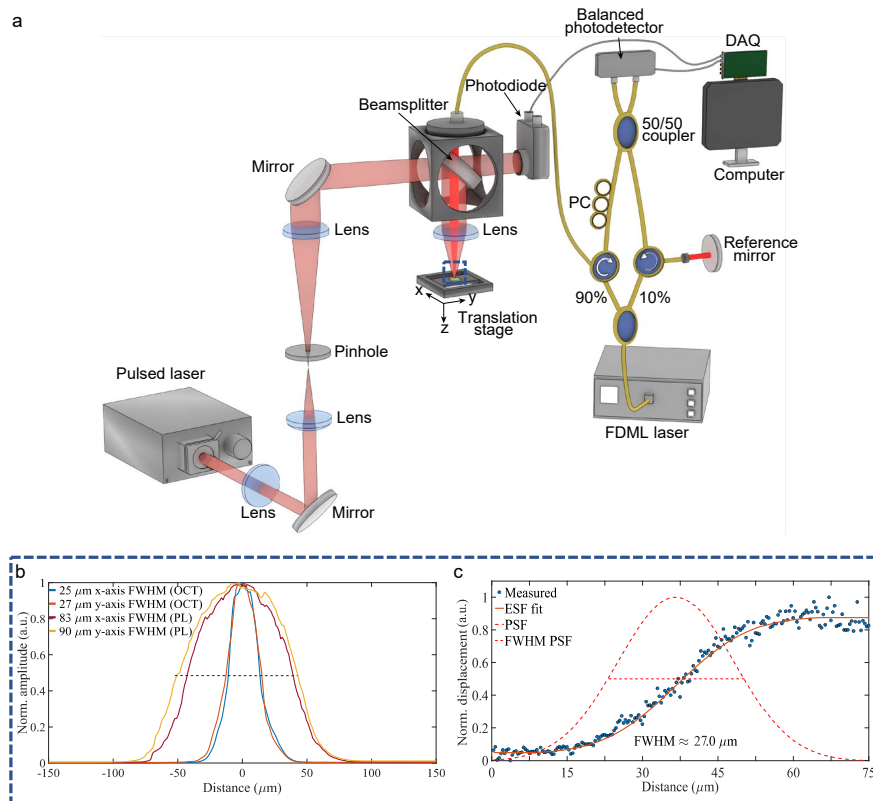

Fig. 1. Schematic of the TE-OCT imaging system. (a) Schematic of the setup based on a wavelength tunable pulsed laser and a 1.6 MHz phase-sensitive OCT system. OCT, optical coherence tomography, FDML, Fourier domain mode locked, PC, polarization controller, DAQ, data acquisition card. (b) Characterization of the overlapping OCT beam and pulsed laser beam and their respective full-width-half-maximum (FWHM) spot sizes. (c) Lateral resolution was measured by scanning the sharp edge of a detector card and fitting the edge spread function (ESF). The point spread function (PSF) was derived from the ESF, with a FWHM lateral resolution of 27.0 µm.

The spot sizes of the co-aligned beams were measured using a dual scanning slit beam profiler (BP209-IR2/M, Thorlabs, U.S.) with spot sizes (FWHM) of 90.0 µm for the pulsed laser and 27.0

µm for the PhS-OCT system (Fig. 1(b)). To characterize the lateral resolution of the TE-OCT system, we fitted the edge-spread function (ESF) acquired by scanning a sharp edge of a laser detector card (VRC2, Thorlabs, U.S.) as shown in Fig. 1(c). The point-spread function (PSF) was then calculated by taking the derivative of the ESF. The lateral resolution measured as the full-width at half-maximum (FWHM) of the PSF, is approximately 27.0 µm. Images of the biological samples were generating by raster scanning a 3-axis translational stage setup (X-LDM110C-AE54D12, Zaber, Canada; KMTS50E/M, Thorlabs, U.S.; LTA-HS, Newport, U.S.). A 200 Hz master clock signal was used to synchronize the movement of the stages, OCT data acquisition, photodiode detection and pulse emission from the pulsed laser.

2.4. Data processing and image reconstruction

For each laser pulse, an M-mode OCT image consisting of 40 A-lines (27 µs duration) for imaging or 80 A-lines (50 µs duration) for spectra study, was acquired to display tissue motion versus time, at one location on the sample. The acquisition of each M-mode image was triggered 8 µs prior to the arrival of the laser pulse. To measure the displacement, the Doppler phase shift was extracted from the M-mode dataset by comparing the phase signal before and after the arrival of the laser pulse. The Doppler phase shift ($\Delta\varphi$) was further converted to tissue displacement following:

$$u(r, z) = \frac{\lambda_0}{4n\pi} \Delta\varphi(r, z) \tag{14}$$

where $u(r, z)$ is the surface displacement at a radial location, r and depth, z, n is the refractive index of the sample, and λ_0 is center wavelength of the OCT laser source.

The surface displacement for each data point on a spectrum or image was found by taking the mean phase of 4 A-lines before the arrival of the pulse and subtracting this from the mean phase value of 4 A-lines following the arrival of the pulse (with a 15-A-line delay after the pulse arrival) which is observed in the M-mode images, giving the absolute change in phase above the noise floor. In the end, each M-mode image produced a new A-line that shows the tissue displacement corresponding to a specific excitation laser pulse. The new A-lines are then combined to produce a 2D TE-OCT image which can be reconstructed to offer a top view of the entire biological sample. To improve the image quality, a filter replaces each pixel with the average of its 3×3 neighborhood. Meanwhile, in the conventional way of OCT data processing, the intensity part of the dataset was used to reconstruct the OCT image that shows the microstructure of the sample with a contrast that relies upon optical reflectance.

2.5. Tissue collection and processing

Tissue samples were acquired from two regions of a porcine right coronary artery (RCA). Each region was cut into two blocks. In block one, adjacent slices were made for histology staining while in block two, a piece of unprocessed tissue was freshly resected, and directly used for TE-OCT imaging without any staining or labelling. Sample acquisition was approved by the local animal welfare committee of the University Medical Centre Utrecht and was executed conforming with the "Guide for the Care and Use of Laboratory Animals". The porcine (Exemplar Genetics LDLr KO 60-80 kg) was fed for 1 year on an atherosclerotic high fat diet containing egg yolk, ground corn, sucrose, sweet butter cream, di-cal-phosphate, lard and limestone.

2.6. Gel wax phantom preparation

Gel wax phantoms were prepared to characterize the TE-OCT prototype. Native gel wax (FF1 003, Mindsets Online, Waltham Cross, UK), was selected as the material of choice as reference data for both the absorption and scattering coefficients are readily available [38]. We mixed the native gel wax with carbon black ink (Cranfield) with concentrations varying from 0.005 to 0.03 w/v, following the procedure described in E. Maneas's work [38]. The native gel wax was then

heated to ~200 °C with continuous magnetic stirring for approximately one hour. The gel wax was then sonicated (Emag 12 HC, Emag, Germany) for 2 minutes then reheated to maintain mobility of the gel wax. This step was repeated once for the transparent phantoms and multiple times for the phantoms with added ink, until the wax-ink solution appeared homogenous. All phantoms were then transferred to a vacuum chamber for degassing to allow any remaining bubbles to float to the surface. Lastly, they were poured into glass containers and allowed to cool to room temperature.

3. Results

TE-OCT relies on the detection of nanometer scale thermo-elastic tissue displacements made possible by a high-speed, PhS-OCT system, in combination with a wavelength tunable nanosecond pulsed laser for sample excitation. The surface movement following irradiation is detected as the Doppler phase shift signal by the OCT system and used to reconstruct thermo-elastic displacement images.

3.1. Characterization of the surface thermo-elastic displacement in gel wax phantoms

We investigated the thermo-elastic (TE) displacement response by recording the signals of mineral-oil rich gel wax phantoms. The experimental results were compared with the theoretical results generated from the 2D model. Figure 2(a) shows the M-mode images acquired from a gel wax phantom with no added absorbing or scattering materials using 1210 nm and 1330 nm excitation wavelengths. The surface displacement was extracted from the M-mode images as seen in Fig. 2(b). The displacement was averaged upon 1000 laser pulses for each wavelength, with a fixed pulse energy of 470 µJ. Displacement is observed at 1210 nm due to the relatively high optical absorption coefficient at this wavelength (1.79 cm^{-1}) [39]. Little to no optical absorption at 1330 nm (0.19 cm^{-1}) by the gel wax phantom leads to a much lower displacement when compared to that of 1210 nm wavelength. It is worth mentioning that no change can be seen in the M-mode OCT images since the displacement is much smaller than the axial resolution of conventional OCT, and it can only be measured by comparing the phase signal.

To investigate the relationship between surface displacement and optical fluence, gel wax phantoms containing no added absorbing or scattering materials were used. We varied the fluence of the pulsed laser and measured the resulting surface displacement at both 1210 nm and 1330 nm wavelengths. The pulsed laser was operated at 10 Hz repetition rate and each displacement measurement at a particular fluence was obtained by averaging 300 measurements and plotted with their corresponding error bars in (Fig. 2(c)). The results show linearity with increased fluence resulting in a corresponding increase in displacement with R^2 values of 1.0 at 1210 nm and 0.984 at 1330 nm.

To characterize the relation between the optical absorption coefficient and surface displacement, we mixed gel wax phantoms with various concentrations of an optical absorber (carbon black ink). Five phantoms with concentrations ranging from 0.005 to 0.03 w/v % were prepared and the surface displacements were measured at 1210 nm and 1330 nm with a fixed pulse energy of 285 µJ. Each displacement was averaged upon 300 measurements. As shown in Fig. 2(d), a linear relationship is found between the surface displacement and the optical absorption, with R^2 values of 0.971 at 1210 nm and 0.993 at 1330 nm.

3.2. Spectroscopic measurements using TE-OCT

To investigate the spectroscopic detection using TE-OCT, we measured the surface displacement of a gel wax phantom while tuning the wavelength of the excitation pulsed laser from 1100 nm to 1500 nm with a 1 nm step size. Each displacement value was obtained by averaging the measurements of 10 laser pulses. As the pulse energy of the pulsed laser gradually decreases going further in the short-wave infrared (SWIR) range, from 1100 nm (650 µJ) to 1500 nm (315
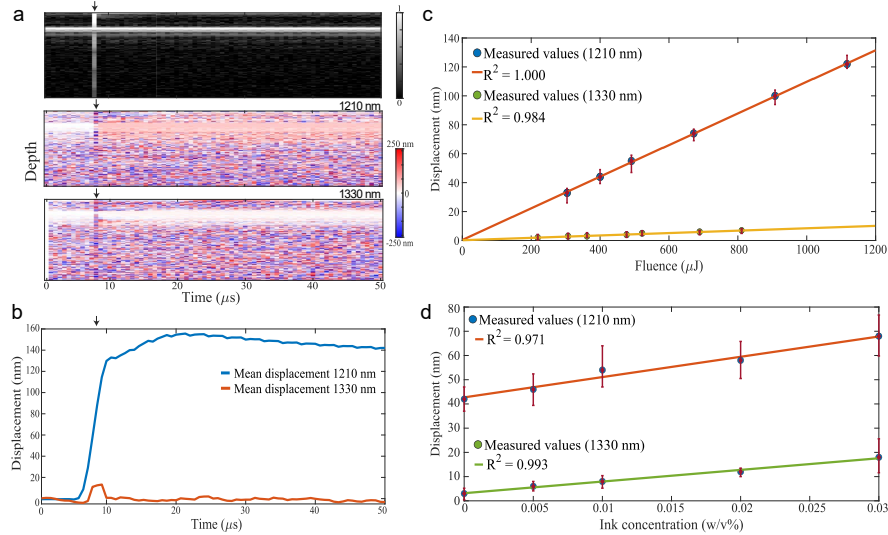
Fig. 2. Characterization of thermo-elastic surface displacement in gel wax phantoms. (a) M-mode OCT images showing the sample structure and displacement before and after pulse arrival (black arrow), at 1210 nm and 1330 nm excitation wavelengths. (b) Surface displacements of gel wax phantom extracted from M-mode OCT images using 1210 nm and 1330 nm excitation laser pulses. (c) Correlation between surface displacement and pulsed laser fluence at 1210 and 1330 nm. (d) Correlation between surface displacement and optical absorption in phantoms containing varying concentrations of carbon black ink at 1210 and 1330 nm

µJ), a photodiode was used to monitor the pulse energy and compensate the spectrum, knowing the linear relationship between displacement and pulse laser fluence. A theoretical TE spectrum was calculated based on the 2D model by assuming negligible scattering and referencing the absorption spectrum of mineral oil from literature [40]. As shown in Fig. 3(a), the surface displacements measured at various wavelengths form a spectrum which is governed by the optical absorption of the phantom. To the details, displacement peaks of methylene in the mineral oil are observed at 1196 and 1210 nm and the combination of methylene and methyl groups at 1390 and 1420 nm are visible. These measured spectral features agree well with the theoretical TE displacement spectrum. As scattering is assumed negligible in the phantom, the 2D model is then dominated by the absorption spectrum of mineral oil with no discernable difference. The strength of the model can be better appreciated when acquiring spectra from porcine lipid containing scattering as shown in Fig. 3(c).

Another variable of interest is the pulsed laser beam spot size and its relationship with fluence and optical penetration depth. To investigate this relationship, TE displacement spectra were acquired over the wavelength range of 1100–1300 nm with 10 pulses averaged per wavelength as shown in Fig. 3(b). The upper and lower limits of each set of 10 pulses per wavelength, were plotted in the shaded area around the mean experimental spectra. The pulsed laser was operated at an energy of 650 µJ per pulse at 1100 nm decreasing to 420 µJ per pulse at 1300 nm. The results show that the displacement magnitude across the spectrum with a 150.0 µm spot size (FWHM) is two times larger compared to that of the spot size (FWHM) of 300.0 µm. This suggests that a smaller spot size and proportionately higher energy density, results in a higher detected signal magnitude. The measured spectra were close to the theoretical spectra and mineral oil optical spectra obtained from literature [40]. A slight mismatch between the
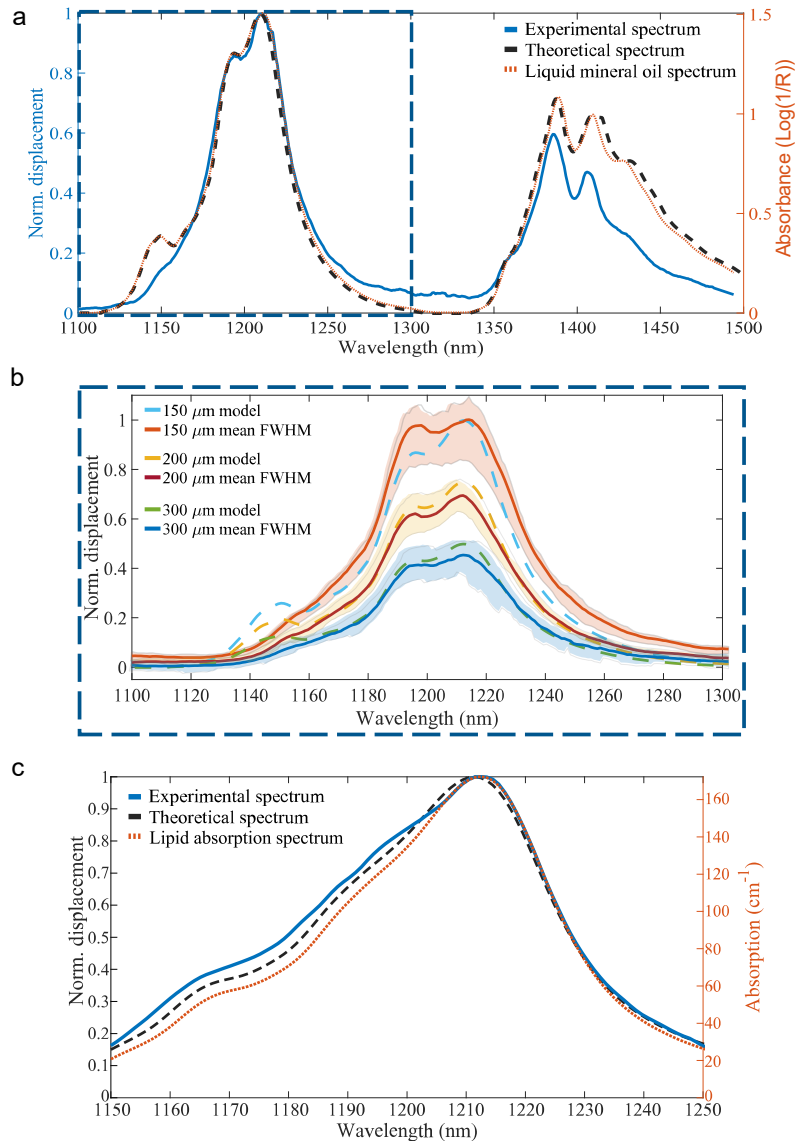
Fig. 3. TE displacement spectra of mineral oil and porcine fat. (a) Comparison between normalized thermo-elastic displacement spectrum, theoretical spectrum, and optical absorption spectrum of mineral oil. (b) Comparison between experimental and theoretical spectra using different spot sizes of the excitation laser pulse. (c) TE displacement spectrum of porcine fat with comparison with theoretical and reference spectra.

experimental spectrum and the theoretical spectrum can be found at 1150 ± 10 nm wavelength. This might be due to slight variations in the refinement of our phantoms versus the referenced pure mineral oil spectrum in literature [40].

3.3.   TE-OCT imaging of porcine coronary arteries

TE-OCT images and spectra were acquired in two regions (region 1 and region 2) of a porcine right coronary artery (RCA) without any staining or labelling. Two TE displacement spectra over

the 1100 - 1850 nm wavelength range were respectively acquired from the coronary artery wall and periadventitial lipid in region 1. Each displacement data point was averaged over 10 pulses with an energy range of 650–235 μJ per pulse. As shown in Fig. 4, different features can be seen between the artery wall and the periadventitial lipid. Specifically, two peaks can be seen at 1210 nm and 1720 nm in the spectrum of periadventitial lipid. This is because of the strong optical absorption of lipid at 1210 and 1720 nm wavelengths agreeing with that of the reference optical absorption spectrum [41]. In contrast, displacement can be seen over the 1400–1525 nm range on the artery wall, which is due to a combination of the optical absorption of collagen, elastin and water at this wavelength range [42,43]. However, in a recent paper by Salimi et al. [44], they report that water, though highly absorbing at 1210 nm, shows little change in optical path length due to its large heat capacity which acts against temperature rise and thermal expansion. This translates to only a small contribution to the measured displacement in the 1450 nm region corresponding to the large absorption peak of water [43]. On one hand, TE-OCT reveals unique spectral features of specific tissue types, while on the other hand, tissue type could possibly be identified in the TE-OCT images by choosing a proper excitation wavelength.
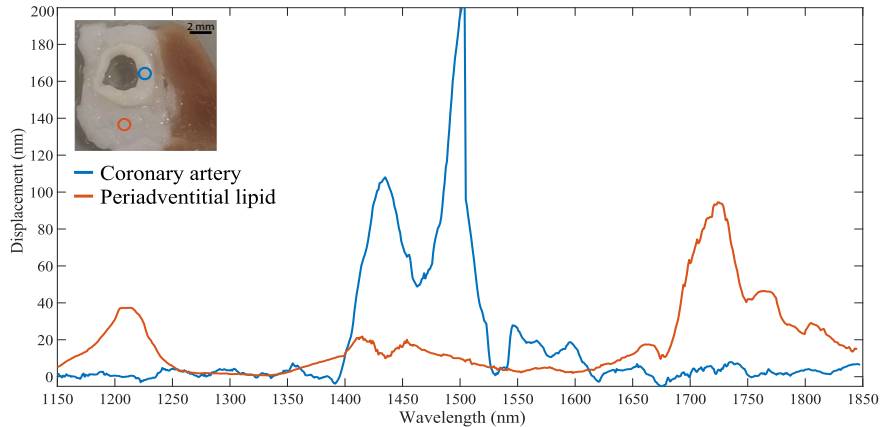

Fig. 4. TE displacement spectra of healthy artery wall and periadventitial lipid in region 1. Two spectra corresponding to the artery wall (highlighted blue on sample) and periadventitial lipid (highlighted orange on sample), over the wavelength range of 1150–1850nm.

2D TE-OCT images were acquired by scanning the coronary artery of region 1 at 1590 and 1720nm, with an excitation energy of ~54 μJ per pulse. A TE-OCT image (10 × 10 mm dimension, 400 × 400 pixels) can be acquired within 13.3 minutes by setting a 25 μm step size of the 2D scanner and a 200 Hz repetition rate of the pulsed laser. As TE-OCT utilizes PhS-OCT detection, the conventional OCT structural image can also be acquired simultaneously. The experimentally acquired TE-OCT images were qualitatively compared to histological samples which were stained using Hematoxylin–Eosin (H&E) for general structure, Oil Red O (ORO) to highlight lipid content and Resorcin–Fuchsin (RF) staining for the collagen-elastin components. The OCT image (Fig. 5(a)) shows the microstructure of the coronary artery which corresponds to structures observed in the H&E stained histology (Fig. 5(b)). However, owing to the low contrast of optical reflectance, conventional OCT images cannot clearly identify tissue type. Figure 5(c) shows the TE-OCT image using 1720nm excitation laser pulses to highlight lipid. The periadventitial lipid shows displacement and can now be clearly identified in the TE-OCT image. This is confirmed by the presence of the dissolved lipids which are seen as red droplets in the ORO histology and indicated by yellow arrows in Fig. 5(d). In addition, displacement is observed
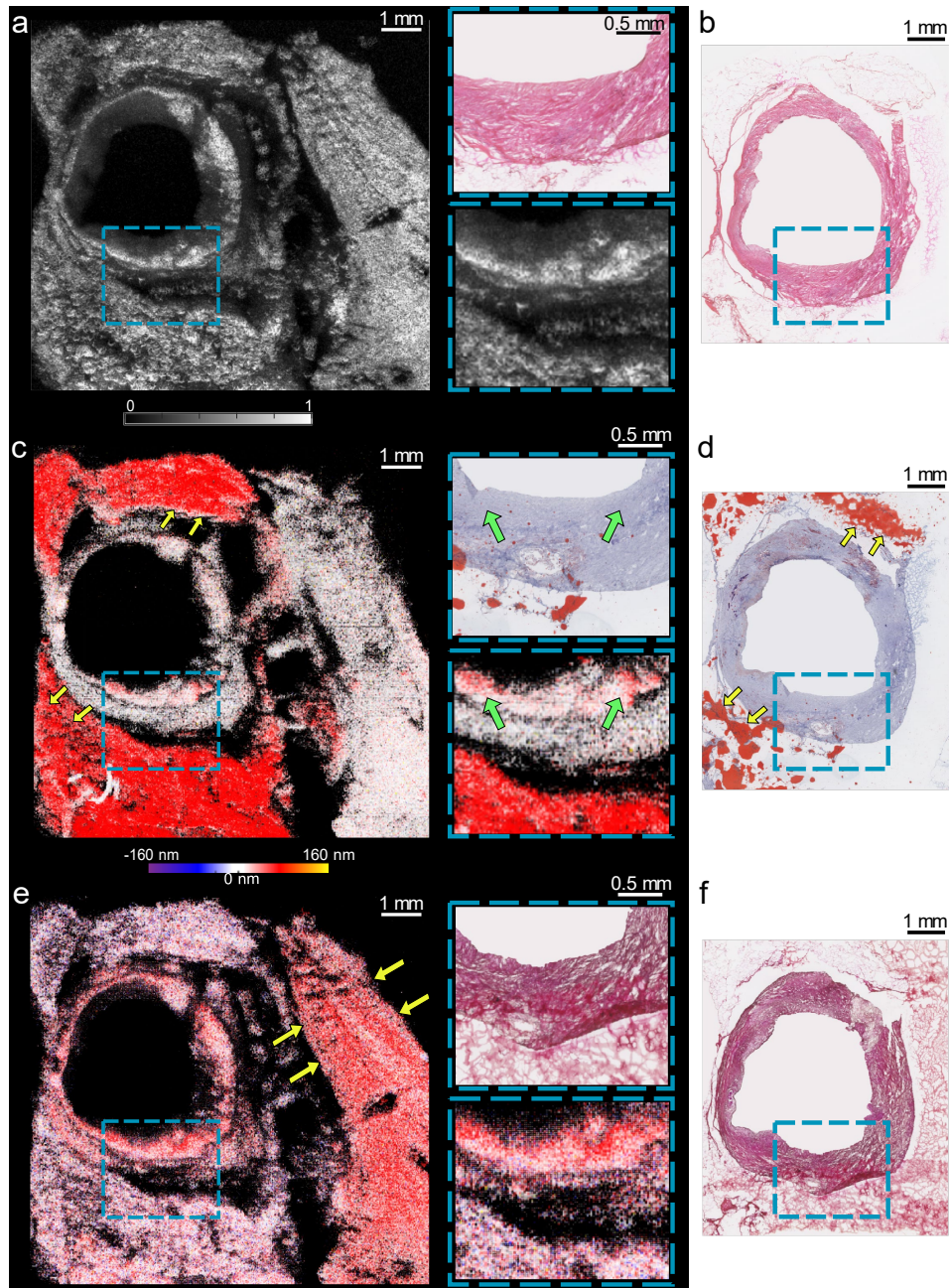
Fig. 5. TE-OCT images of coronary artery (region1) compared to histology. (a) Conventional OCT image of coronary artery. (b) H&E-stained histology of coronary artery. (c) Surface displacement image of artery excited at 1720nm. (d) ORO-stained section of coronary artery. (e) Surface displacement with 1590 nm excitation. (f) RF-stained section of coronary artery.

on the artery wall (green arrows) as shown in the magnified part in Fig. 5(c) as compared to Fig. 5(d). This is likely due to the polarity of the lipids as ORO staining only highlights non-polar

lipids. The lipid area near 11 - 13 o'clock was not observed in the TE-OCT image. That is because the low OCT intensity signal led to a relatively large phase noise, and the signal was filtered out after a 3×3 pixel smoothing. Moving to a 1590 nm excitation wavelength, surface displacement is now observed on the artery wall where collagen and elastin are highlighted as shown in Fig. 5(e). This is confirmed in Fig. 5(f) which shows the RF-stained histology highlighting the collagen-elastin tissue component in red. In addition, displacement signal was detected in the myocardium indicated by the yellow arrows (Fig. 5(e)), which is due to optical absorption of cardiac muscle.

A TE displacement spectrum was also acquired in an atherosclerotic plaque from region 2 of the same RCA as shown in Fig. 6. The spectrum shows complex features as a combination of spectral features of the artery wall and periadventitial lipid. More specifically, displacement can be seen at 1210 nm, 1720nm and across the 1400–1525 nm wavelength range. This result suggests that the displacement is contributed by both lipid and collagen tissue components.

TE-OCT images of the atherosclerotic plaque of region 2 were acquired at 1590 and 1720 nm wavelengths. The conventional OCT image shows the structure of the artery wall (Fig. 7(a)) which is comparable to the H&E histology (Fig. 7(b)). Slightly stronger OCT signal can be seen at 5 o'clock (blue dashed box), 9 o'clock (yellow dashed box) and in the periadventitial tissue (green dashed box) compared to other areas in the image. This may be due to the relatively high optical reflectance of the lipid component. However, the OCT image feature interpretations are not sufficient to identify lipid tissue. Figure 7(c) shows the TE-OCT image acquired by using 1720 nm pulse laser excitation. Again, displacement can be seen in the periadventitial lipid (green dashed box), which is confirmed by the lipid laden areas (red droplets indicated by yellow arrows) in the ORO histology (Fig. 7(d)). In addition, two lipid-rich areas can be seen in the magnified parts, one in the yellow box and another in the blue box, both of which are confirmed by the ORO histology (yellow and blue boxes in Fig. 7(d)). Switching the excitation wavelength to 1590 nm, the collagen-elastin tissue components are highlighted, as shown in Fig. 7(e). In the magnified parts of Fig. 7(e), the image features are different from Fig. 7(c). In the periadventitial lipid (green box in Fig. 7(e)), there is no longer a discernible signal compared to the same location using 1720 nm excitation. Displacement can be observed in the lipid-rich area (yellow and blue boxes), however, this is now mainly due to the collagen and elastin tissue
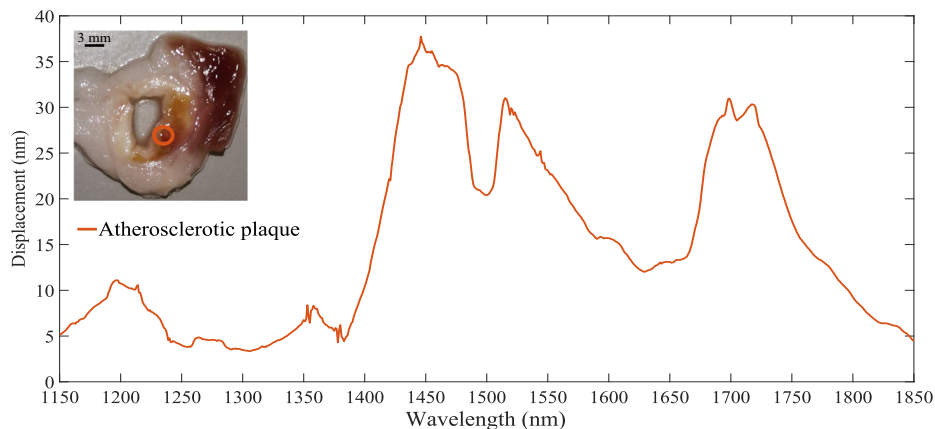

Fig. 6. TE displacement spectrum acquired from atherosclerotic plaque in region2 of the RCA. Spectrum corresponding to the atherosclerotic plaque on artery wall (highlighted orange in sample), over the wavelength range of 1150–1850nm.
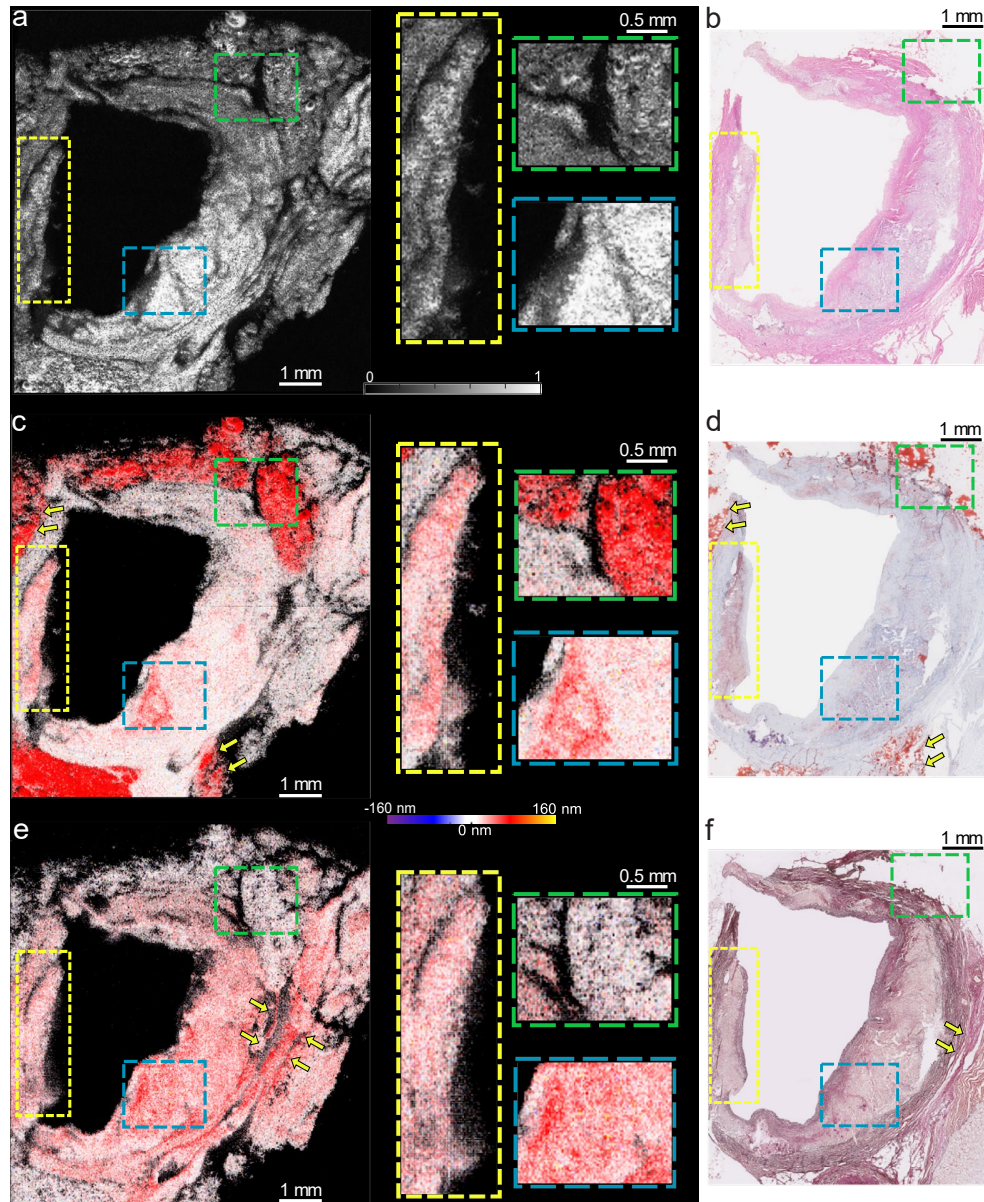
Fig. 7. TE-OCT image analysis of atherosclerotic plaque (region 2) compared with histology. (a) Conventional OCT image of artery. (b) H&E-stained histology of coronary artery. (c) Surface displacement of artery at 1720nm. (d) ORO-stained section of coronary artery. (e) Surface displacement at 1590 nm. (f) RF-stained section of coronary artery

components. In addition, collagen bands are observed on the outer wall of the sample which are highlighted by the yellow arrows in Fig. 7(e). In all cases, the collagen-elastin components are confirmed by the RF histology as shown in the corresponding locations in Fig. 7(f). Therefore, both lipid and collagen-elastin tissue components of the atherosclerotic plaques can be identified by TE-OCT with histology confirmation, which also agrees with our previous analysis of the TE-OCT spectrum features.

4. Discussion

We demonstrate spectroscopic TE-OCT as a new tool in optical imaging which utilizes the laser-tissue interaction basis of PAI, and the technical advantages of PhS-OCT. TE-OCT can simultaneously visualize tissue microstructure as in conventional OCT and identify tissue components as in PAI. The experimentally acquired TE displacement spectra show good agreement with that of the analytical model and reference optical absorption spectra. TE-OCT provides imaging in an all-optical, non-contact and label-free form offering potential advantages for biomedical applications by eliminating the need for a contact medium as is required in transducer-based PAI [45]. Furthermore, the demonstration of optical absorption contrast imaging in porcine coronary artery samples ex vivo, with identification of lipid and collagen content offers a substantial increase in functionality over stand-alone OCT [46–48]. In addition, TE-OCT can be practically achieved by improving most of the existing OCT platforms without facing the difficulties of system integration.

PT-OCT is a well-known, related development, which relies on PhS-OCT to detect thermal expansion induced by optical absorption. Until recently, PT-OCT relied on CW sources, which has led to progressive heat build-up in tissue. The introduction of modulated PT-OCT alleviated this limitation [49,50]. PT-OCT has also been used in lipid imaging in coronary arteries [51]. Compared to these recent PT-OCT studies, our study focused on extracting spectroscopic information from thermoelastic displacement. Since the thermoelastic displacement happens within a few microseconds, TE-OCT can achieve spectroscopic imaging, which however requires a MHz A-line acquisition rate and relatively expensive pulsed laser, as opposed to the kHz A-line rate and relatively low-power and low-cost laser used in PT-OCT. Spectroscopic OCT can extract optical spectroscopic information of tissue, but the features are limited to the wavelength range of the OCT laser source. In contrast, Spectroscopic TE-OCT relies upon the wavelength tuning range of the pulsed laser which can achieve a larger range than that of the OCT laser source.

Our current TE-OCT prototype does suffer from several technical limitations. First, the pulsed laser used for excitation has a maximum repetition rate of 200 Hz. This results in an acquisition and processing time of 13.4 minutes for a 400×400 pixel TE-OCT image. In principle, the 1.6 MHz FDML OCT system, can support a laser pulse repetition rate of up to 30 kHz, which can potentially generate a TE-OCT image within 5.3 s. In the future, we would employ a faster pulsed laser, thus, increasing the imaging speed. Second, the resolution of TE-OCT depends mainly upon the spot size of the OCT beam while the excitation area is determined by the spot size of the pulsed laser. In the current system, the laser fluence induces a temperature rise on the order of millikelvin from each pulse as is the same for photoacoustic imaging. Though the effect on tissue heating is reduced by energy deposition on a nanosecond scale [52], tissue damage can occur due to repetitive pulse illumination. In the future, we will further reduce the spot sizes of both the pulsed laser beam and the OCT beams to achieve better resolution and higher excitation efficiency. Third, our current study has been focused on surface imaging of the tissue specimen, but it is possible to advance the study towards volumetric three-dimensional (3D) imaging. In the future, we will investigate a 3D model to determine tissue motion along the full depth of the interrogation beam. Characterization of tissue structure and composition in the entire 3D imaging volume may further enable catheter or handheld-probe-based imaging applications.

5. Conclusion

In this work, we have demonstrated and characterized spectroscopic TE-OCT, an optical imaging modality which can simultaneously acquire co-registered images containing structure and tissue-specific information in a label-free, non-contact form. The experimental data acquired in this study agrees well with the theoretical data calculated using a 2D model. Preliminary results of coronary artery samples show that lipid and collagen tissue components can be identified in both

imaging and TE displacement spectra. We believe that spectroscopic TE-OCT could become a useful optical imaging tool for biomedical research, with the possibility of extending TE-OCT towards pathology, cardiology, and endoscopic imaging.

Disclosures. Robert Huber has a financial interest in Optores Gmbh, which commercializes FDML technology. The other co-authors declare no competing interest.

Data Availability. Data underlying the results presented in this paper are not publicly available at this time but may be obtained from the corresponding authors upon request.

References

1. J. W. Lichtman and J.-A. Conchello, "Fluorescence microscopy," Nat. Methods **2**(12), 910–919 (2005).
2. A. F. Palonpon, M. Sodeoka, and K. Fujita, "Molecular imaging of live cells by Raman microscopy," Curr. Opin. Chem. Biol. **17**(4), 708–715 (2013).
3. G. Scarcelli and S. H. Yun, "Confocal Brillouin microscopy for three-dimensional mechanical imaging," Nat. Photonics **2**(1), 39–43 (2008).
4. P. J. Caspers, G. W. Lucassen, and G. J. Puppels, "Combined In Vivo Confocal Raman Spectroscopy and Confocal Microscopy of Human Skin," Biophys. J. **85**(1), 572–580 (2003).
5. J. W. Kang, N. Lue, C.-R. Kong, I. Barman, N. C. Dingari, S. J. Goldfless, J. C. Niles, R. R. Dasari, and M. S. Feld, "Combined confocal Raman and quantitative phase microscopy system for biomedical diagnosis," Biomed. Opt. Express **2**(9), 2484 (2011).
6. W. Zhang, Y. Li, V. P. Nguyen, Z. Huang, Z. Liu, X. Wang, and Y. M. Paulus, "High-resolution, in vivo multimodal photoacoustic microscopy, optical coherence tomography, and fluorescence microscopy imaging of rabbit retinal neovascularization," Light Sci. Appl. **7**(1), 103 (2018).
7. P. L. Choyke, R. Alford, H. M. Simpson, J. Duberman, G. Craig Hill, M. Ogawa, C. Regino, and H. Kobayashi, "Toxicity of organic fluorophores used in molecular imaging: Literature review," Mol. Imaging **8**(6), 341–354 (2009).
8. C. Vinegoni, I. Botnaru, E. Aikawa, M. A. Calfon, Y. Iwamoto, E. J. Folco, V. Ntziachristos, R. Weissleder, P. Libby, and F. A. Jaffer, "Indocyanine Green Enables Near-Infrared Fluorescence Imaging of Lipid-Rich, Inflamed Atherosclerotic Plaques," Sci. Transl. Med. **3**(84), 84ra45 (2011).
9. S. Wang, X. Li, S. Y. Chong, X. Wang, H. Chen, C. Chen, L. G. Ng, J. W. Wang, and B. Liu, "In Vivo Three-Photon Imaging of Lipids using Ultrabright Fluorogens with Aggregation-Induced Emission," Adv. Mater. **33**(11), 2007490 (2021).
10. A. D'Aléo, A. Bourdolle, S. Brustlein, T. Fauquier, A. Grichine, A. Duperray, P. L. Baldeck, C. Andraud, S. Brasselet, and O. Maury, "Ytterbium-based bioprobes for near-infrared two-photon scanning laser microscopy imaging," Angew. Chemie - Int. Ed. **51**(27), 6622–6625 (2012).
11. J. Aguirre, M. Schwarz, N. Garzorz, M. Omar, A. Buehler, K. Eyerich, and V. Ntziachristos, "Precision assessment of label-free psoriasis biomarkers with ultra-broadband optoacoustic mesoscopy," Nat, Biomed. Eng. **1**(5), 1–8 (2017). .
12. H. F. Zhang, K. Maslov, G. Stoica, and L. V. Wang, "Functional photoacoustic microscopy for high-resolution and noninvasive in vivo imaging," Nat. Biotechnol. **24**(7), 848–851 (2006).
13. M. S. Feld, C. von Rosenberg, L. T. Perelman, M. L. Dark, I. Itzkan, and D. Albagli, "The thermoelastic basis of short pulsed laser ablation of biological tissue," Proc. Natl. Acad. Sci. **92**(6), 1960–1964 (1995).
14. K. Maslov, H. F. Zhang, S. Hu, and L. V. Wang, "Optical-resolution photoacoustic microscopy for in vivo imaging of single capillaries," Opt. Lett. **33**(9), 929 (2008).
15. H. W. Wang, N. Chai, P. Wang, S. Hu, W. Dou, D. Umulis, L. V. Wang, M. Sturek, R. Lucht, and J. X. Cheng, "Label-free bond-selective imaging by listening to vibrationally excited molecules," Phys. Rev. Lett. **106**(23), 259901 (2011).
16. H. C. Zhou, N. Chen, H. Zhao, T. Yin, J. Zhang, W. Zheng, L. Song, C. Liu, and R. Zheng, "Optical-resolution photoacoustic microscopy for monitoring vascular normalization during anti-angiogenic therapy," Photoacoustics **15**>(1), 238106 (2019).
17. H. Zhao, G. Wang, R. Lin, X. Gong, L. Song, T. Li, W. Wang, K. Zhang, X. Qian, H. Zhang, L. Li, Z. Liu, and C. Liu, "Three-dimensional Hessian matrix-based quantitative vascular imaging of rat iris with optical-resolution photoacoustic microscopy in vivo," J. Biomed. Opt. **23**(04), 1 (2018).
18. Q. Zhao, R. Lin, C. Liu, J. Zhao, G. Si, L. Song, and J. Meng, "Quantitative analysis on in vivo tumor-microvascular images from optical-resolution photoacoustic microscopy," J. Biophotonics **12**(6), e201800421 (2019).
19. M. Xiao, C. Dai, L. Li, C. Zhou, and F. Wang, "Evaluation of retinal pigment epithelium and choroidal neovascularization in rats using laser-scanning optical-resolution photoacoustic microscopy," Ophthalmic Res. **63**(3), 271–283 (2020).

20. T. Buma, N. C. Conley, and S. W. Choi, "Multispectral photoacoustic microscopy of lipids using a pulsed supercontinuum laser," Biomed. Opt. Express **9**(1), 276 (2018).
21. P. Hajireza, W. Shi, K. Bell, R. J. Paproski, and R. J. Zemp, "Non-interferometric photoacoustic remote sensing microscopy," Light Sci. Appl. **6**(6), e16278 (2017).
22. I. K. Jang, *Cardiovascular OCT Imaging* (Springer International Publishing, 2015).
23. J. E. Freund, M. Buijs, C. D. Savci-Heijink, D. M. de Bruin, J. J. M. C. H. de la Rosette, T. G. van Leeuwen, and M. P. Laguna, "Optical Coherence Tomography in Urologic Oncology: a Comprehensive Review," SN Compr Clin. Med. **1**(2), 67–84 (2019).
24. A. López-Marín, G. Springeling, R. Beurskens, H. van Beusekom, A. F. W. van der Steen, A. D. Koch, B. E. Bouma, R. Huber, G. van Soest, and T. Wang, "Motorized capsule for shadow-free OCT imaging and synchronous beam control," Opt. Lett. **44**(15), 3641 (2019).
25. N. Minakaran, E. R. de Carvalho, A. Petzold, and S. H. Wong, "Optical coherence tomography (OCT) in neuro-ophthalmology," Eye **35**(1), 17–32 (2021).
26. K. Karnowski, A. Ajduk, B. Wieloch, S. Tamborski, K. Krawiec, M. Wojtkowski, and M. Szkulmowski, "Optical coherence microscopy as a novel, non-invasive method for the 4D live imaging of early mammalian embryos," Sci. Rep. **7**(1), 416–512 (2017).
27. J. Zhu, H. R. Freitas, I. Maezawa, L. Jin, and V. J. Srinivasan, "1700nm optical coherence microscopy enables minimally invasive, label-free, in vivo optical biopsy deep in the mouse brain," Light Sci. Appl. **10**(1), 145 (2021).
28. J. F. de Boer, C. K. Hitzenberger, and Y. Yasuno, "Polarization sensitive optical coherence tomography – a review [Invited]," Biomed. Opt. Express **8**(3), 1838 (2017).
29. H. S. Nam and H. Yoo, "Spectroscopic optical coherence tomography: A review of concepts and biomedical applications," Appl. Spectrosc. Rev. **53**(2-4), 91–111 (2018).
30. C. G. Rylander, D. P. Davé, T. Akkin, T. E. Milner, K. R. Diller, and A. J. Welch, "Quantitative phase-contrast imaging of cells with phase-sensitive optical coherence microscopy," Opt. Lett. **29**(13), 1509 (2004).
31. R. K. Wang and A. L. Nuttall, "Phase-sensitive optical coherence tomography imaging of the tissue motion within the organ of Corti at a subnanometer scale: a preliminary study," J. Biomed. Opt. **15**(5), 056005 (2010).
32. J. M. Tucker-Schwartz, T. A. Meyer, C. A. Patil, C. L. Duvall, and M. C. Skala, "In vivo photothermal optical coherence tomography of gold nanorod contrast agents," Biomed. Opt. Express **3**(11), 2881 (2012).
33. T. Wang, T. Pfeiffer, M. Wu, W. Wieser, G. Amenta, W. Draxinger, A. F. W. van der Steen, R. Huber, and G. van Soest, "Thermo-elastic optical coherence tomography," Opt. Lett. **42**(17), 3466 (2017).
34. M. L. Dark, L. T. Perelman, I. Itzkan, J. L. Schaffer, and M. S. Feld, "Physical properties of hydrated tissue determined by surface interferometry of laser-induced thermoelastic deformation," Phys. Med. Biol. **45**(2), 529–539 (2000).
35. L. D. Landau, E. M. Lifshitz, A. M. Kosevich, L. P. Pitaevskii, J. B. Sykes, and W. H. Reid, "Course of Theoretical Physics, vol. 7 - Theory of Elasticity," **7**, 195 (1986).
36. D. Albagli, M. Dark, C. von Rosenberg, L. Perelman, I. Itzkan, and M. S. Feld, "Laser-induced thermoelastic deformation: A three-dimensional solution and its application to the ablation of biological tissue," Med. Phys. **21**(8), 1323–1331 (1994).
37. T. Wang, T. Pfeiffer, J. Daemen, F. Mastik, W. Wieser, A. F. W. Van Der Steen, R. Huber, and G. Van Soest, "Simultaneous Morphological and Flow Imaging Enabled by Megahertz Intravascular Doppler Optical Coherence Tomography," IEEE Trans. Med. Imaging **39**(5), 1535–1544 (2020).
38. E. Maneas, W. Xia, O. Ogunlade, M. Fonseca, D. I. Nikitichev, A. L. David, S. J. West, S. Ourselin, J. C. Hebden, T. Vercauteren, and A. E. Desjardins, "Gel wax-based tissue-mimicking phantoms for multispectral photoacoustic imaging," Biomed. Opt. Express **9**(3), 1151 (2018).
39. K. Wang, W. Wen, Y. Wang, K. Wang, J. He, J. Wang, P. Zhai, Y. Yang, and P. Qiu, "Order-of-magnitude multiphoton signal enhancement based on characterization of absorption spectra of immersion oils at the 1700-nm window," Opt. Express **25**(6), 5909 (2017).
40. P. A. Picouet, P. Gou, R. Hyypiö, and M. Castellari, "Implementation of NIR technology for at-line rapid detection of sunflower oil adulterated with mineral oil," J. Food Eng. **230**, 18–27 (2018).
41. J. Hui, R. Li, E. H. Phillips, C. J. Goergen, M. Sturek, and J. X. Cheng, "Bond-selective photoacoustic imaging by converting molecular vibration into acoustic waves," Photoacoustics **4**(1), 11–21 (2016).
42. S. K. V. Sekar, I. Bargigia, A. D. Mora, P. Taroni, A. Ruggeri, A. Tosi, A. Pifferi, and A. Farina, "Diffuse optical characterization of collagen absorption from 500 to 1700nm," J. Biomed. Opt. **22**(1), 015006 (2017).
43. C. P. Fleming, J. Eckert, E. F. Halpern, J. A. Gardecki, and G. J. Tearney, "Depth resolved detection of lipid using spectroscopic optical coherence tomography," Biomed. Opt. Express **4**(8), 1269 (2013).
44. M. H. Salimi, M. Villiger, and N. Tabatabaei, "Effects of lipid composition on photothermal optical coherence tomography signals," J. Biomed. Opt. **25**(12), 120501 (2020).
45. J. Yao and L. V. Wang, "Photoacoustic microscopy," Laser Photonics Rev. **7**(5), 758–778 (2013).
46. Y. Chen, "Cellular resolution ex vivo imaging of gastrointestinal tissues with optical coherence microscopy," J. Biomed. Opt. **15**(1), 016025 (2010).
47. P. J. Marchand, A. Bouwens, D. Szlag, D. Nguyen, A. Descloux, M. Sison, S. Coquoz, J. Extermann, and T. Lasser, "Visible spectrum extended-focus optical coherence microscopy for label-free sub-cellular tomography," Biomed. Opt. Express **8**(7), 3343 (2017).

48. A. Lichtenegger, D. J. Harper, M. Augustin, P. Eugui, M. Muck, J. Gesperger, C. K. Hitzenberger, A. Woehrer, and B. Baumann, "Spectroscopic imaging with spectral domain visible light optical coherence microscopy in Alzheimer's disease brain samples," Biomed. Opt. Express **8**(9), 4007 (2017).
49. M. H. Salimi, M. Villiger, and N. Tabatabaei, "Transient-mode photothermal optical coherence tomography," Opt. Lett. **46**(22), 5703 (2021).
50. J. Wu, N. Wu, P. Tang, J. Lin, Y. Lian, and Z. Tang, "Pulse photothermal optical coherence tomography for multimodal hemodynamic imaging," Opt. Lett. **46**(22), 5635 (2021).
51. N. Katta, A. Cabe, T. Hoyt, A. B. McElroy, M. Feldman, and T. Milner, "Detection Of Lipid In Coronary Arteries Using Photothermal Optical Coherence Tomography," J. Am. Coll. Cardiol. **73**(9), 1421 (2019).
52. L. V. Wang, "Optical-Thermal Response of Laser-Irradiated Tissue," in *Optical-Thermal Response of Laser-Irradiated Tissue* (Springer Netherlands, 2011), pp. 743–760.